Solid Earth

Cross-scale strain analysis in the Afar rift (East Africa) from automatic fault mapping and geodesy

Alessandro La Rosa[1,2]**, Pauline Gayrin**[1,3]**, Sascha Brune**[1,3]**, Carolina Pagli**[2]**, Ameha A. Muluneh**[4,1]**, Gianmaria Tortelli**[5]**, and Derek Keir**[5,6]

[1]GFZ Helmholtz Centre for Geosciences, Telegrafenberg, 14473 Potsdam, Germany
[2]Dipartimento di Scienze della Terra, Università di Pisa, Via S. Maria, 53, 56126 Pisa, Italy
[3]Institute of Geosciences, University of Potsdam, Potsdam, Germany
[4]MARUM Center for Marine Environmental Sciences, University of Bremen, Bremen, Germany
[5]Dipartimento di Scienze della Terra, Università degli Studi di Firenze, Via G. La Pira, 4, 50121 Florence, Italy
[6]School of Ocean and Earth Science, University of Southampton, European Way, Southampton, SO16 3ZH, UK

Correspondence: Alessandro La Rosa (alessandro.larosa@dst.unipi.it)

Abstract. The formation of continental rift systems is characterised by the interplay of magmatic and tectonic processes. Their evolution involves a wide range of timescales, from centennial scales of the seismic and diking cycles to strain localisation during millions of years of continental thinning. Our understanding of rift processes at different spatial and timescales is limited by relatively short temporal coverages of geophysical measurements and by spatially discontinuous geological datasets. Here we propose a novel method for the automatic extraction of faults and the calculation of time-averaged strains distributions using topographic information from digital elevation models (DEMs). We apply this method to map ∼ 4000 individual faults within a ∼ 70 000 km^2 area of the Afar rift (East Africa), where the Nubian, Arabian and Somalian plates diverge. By comparing our results to rock dating and recent decadal geodetic measurements, we deduce the rift's deformation history since 4.5 Ma and study its relationship with the current tectonic and magmatic activity. We show that the external portions of the Central Afar rift are not the main locus of strain. Rifting processes have migrated toward the axis where magma emplacement focusses strain due to the mechanical and thermal weakening of the crust. Increasing strains toward north-west suggest a progressive migration of the rifting process in the same direction. Conversely, Southern Afar is characterised by two systems of cross-cutting faults that respond to different strain regimes driven by the separations of the Arabian and Somalian plates from Nubia. This study demonstrates the capacity of our new method in quantifying fault activity and strain distribution in extensional settings and provides new insights into the spatial and temporal evolution of rifting in Afar.

1 Introduction

Rifting of continents is characterised by the interplay between faulting due to the mechanical stretching of the lithosphere and the production and intrusion of magma. These processes are highly variable across spatial and temporal scales. During rifting, magma and tensile strains accumulate in the lithosphere to be released by dike intrusions and/or faulting during cycles that last hundreds to thousands of years (e.g. Ebinger et al., 2010; Wright et al., 2012). The locus of extension may shift during rifting, with progressive in-rift strain focusing or rift jumps mainly controlled by plate tectonic interactions and motions of magma at depth (e.g. Wood, 1983; Wolfenden et al., 2004; Corti et al., 2019; Tortelli et al., 2022; Brune et al., 2023). As such, understanding the evolution of continental rift systems requires investigation of magmatic and tectonic processes at a range of spatial and temporal scales. Geodesy (e.g. InSAR and GPS) can measure the surface expressions of these processes at the regional scale, with millimetre accuracy, and on decadal timescales (e.g.

Biggs et al., 2009; Metzger and Jónsson, 2014; Pagli et al., 2014; Doubre et al., 2017; Moore et al., 2021; La Rosa et al., 2024), yet resolving the accumulation and release of strain in the lithosphere over longer timescales requires geological observations (Wright et al., 2012, Ebinger et al., 2023). According to this aim, the analysis of faults forming in age-constrained rocks can be used to quantify rift deformation over geological timescales (e.g. Dumont et al., 2017; Riedl et al., 2022).

Fault mapping from satellite-based images allows for high-resolution investigation of regional-scale networks. Well-preserved, surface expressions of normal faults in digital elevation models (DEMs) of rifted areas can be used to retrieve the horizontal and vertical components of extension. However, manual fault mapping at the whole rift scale can be time-consuming and prone to interpretation biases. To overcome these limitations, various automatic or semi-automatic methods for fault mapping have recently been developed (e.g. Zielke et al., 2010; Stewart et al., 2018; Gianpietro et al., 2021; Mattéo et al., 2021; Scott et al., 2021). The algorithms developed by Zielke et al. (2010) and Stewart et al. (2018), for example, allow for automatic fault detection and the measurement of lateral and vertical displacements by exploiting geomorphological offset (e.g. rivers). Scott et al. (2021) developed a tool for the semi-automatic fault detection and scarp height estimation using length and slope information calibrated from manually mapped faults. Mattéo et al. (2021) instead used a U-Net convolutional neural network method to automatically detect fractures and faults in both optical imagery and DEMs.

Here we use the Python-based Fault Analysis Toolbox (Fatbox) originally developed by Wrona et al. (2022). Fatbox can detect individual faults in different types of raster data and has previously been applied to automated interpretations of seismic datasets (Wrona et al., 2023), numerical models (Neuharth et al., 2022) and DEMs (Gayrin et al., 2025b) by means of edge detection algorithms. Here, we extended the Fatbox-based workflow for detecting normal faults in DEMs by implementing two workflows for the filtering of artefacts and the calculation of minimum total strains from the horizontal components of fault. Our method was applied to the Afar rift (East Africa) to reconstruct the distribution of strain in the central and southern sector of the rift during the last ~ 4.5 Myr. The Afar rift is the ideal place for this kind of application as the arid environment and associated low erosion rates preserve fault scarps (Dumont et al., 2017). Until now, analysis of strain accumulation and release in Afar has been limited by the relatively short time window of geodetic techniques (e.g. Ruegg et al., 1984; Calais et al., 2008; Pagli et al., 2014; Doubre et al., 2017), while the strain distribution over geological timescales has been investigated only in some sectors of the rift (e.g. the eastern-central Afar) and at low resolution (~ 20 km, Polun et al., 2018). Long-term and regional strain patterns are therefore poorly understood. To address this issue, we combined measurements of minimum total strains with rock dating (Courtillot et al., 1984; Kidane et al., 2003; Lahitte et al., 2003; Feyissa et al., 2019), first to retrieve time-averaged geological rates of deformation (e.g. Riedl et al., 2022) and second to compare our results with geodetically derived strain rates between 2014–2021 (Muluneh et al., 2024; La Rosa et al., 2024). Our approach allowed us to reconstruct the progressive migration of extension from external sectors of the rift, now inactive, toward discrete axial magmatic segments.

2 Geological setting

The Afar rift is a triangular depression resulting from the separation of the Arabian, Somalian and Nubian plates (Fig. 1a). Rifting in the region started in the Gulf of Aden at ~ 35 Ma (Leroy et al., 2004). Rifting in Afar began approximately 30 Ma around the same time as the impingement of a mantle plume and associated eruption of flood basalts (Rime et al., 2023). The Red Sea started opening at ~ 19 Ma, and the northern Main Ethiopian Rift initiated at ~ 11 Ma (Manighetti et al., 1998; Leroy et al., 2004; Wolfenden et al., 2004, 2005; Boone et al., 2021; Rime et al., 2023). The tectonic evolution of Afar prior to ~ 11 Ma was hence dominated by the north-east-directed extensional regime caused by the motion of the Arabian plate (Wolfenden et al., 2004; Maestrelli et al., 2022). At ~ 11 Ma, the northern Main Ethiopian Rift started its northward migration, accommodating the eastward separation of Somalia in Southern Afar. At the same time a westward jump of the southern Red Sea into Afar led to the separation of the Danakil Block that caused the progressive opening of the Central and Northern sectors of Afar (Eagles et al., 2002; McClusky et al., 2010; Rime et al., 2023). Since then, the rifting process in Central Afar and Northern Afar was characterised by a progressive in-rift localisation of extension. Present-day kinematic models of plate spreading from GPS measurements show the Somalian plate currently separating from Nubia at ~ 5 mm yr^{-1} in the ESE–WNW direction (Birhanu et al., 2016; Stamps et al., 2020), while the NE-directed separation of Arabia from Nubia occurs at a rate of ~ 18 mm yr^{-1} (Viltres et al., 2022). In between Arabia and Nubia, the Danakil block is separating from Nubia with the velocity increasing from ~ 10 mm yr^{-1} at latitude 14.5° N to ~ 18 mm yr^{-1} at latitude 12.7° N, exhibiting an anti-clockwise rotation (McClusky et al., 2010; Viltres et al., 2020, 2022).

Rifting in Afar was accompanied by two further major phases of basaltic eruptions (Tortelli et al., 2022) during ~ 4.5–2.5 Ma (Lower Stratoids series) and ~ 2.5–1.2 Ma (Upper Stratoids series) that covered almost the entire region (Fig. 1b). Recent geochemical studies suggest that these two events resulted from a north-eastward shift of strain and volcanism after a jump of the rift in Central Afar, likely induced by the inland propagation of the western Gulf of Aden branch into the Gulf of Tadjoura (Fig. 1a) between
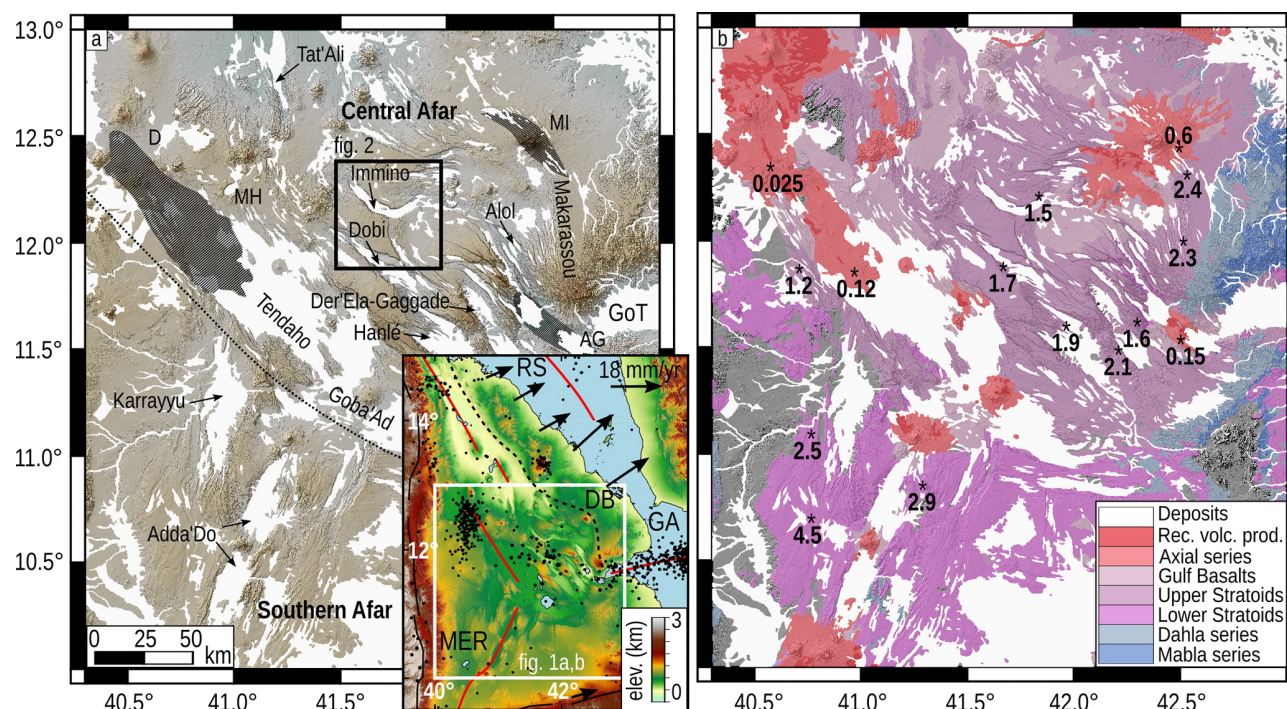
Figure 1. Geological and tectonic setting of Afar. **(a)** 30 m digital elevation model (FABDEM V1-2, Hawker et al., 2022), current axial magmatic segments (black dashed areas) and major grabens in the study area. The black dashed line separates the Central and Southern Afar sectors. The inset in **(a)** shows the current plate kinematics characterising Afar in a Nubia-fixed reference frame (black arrows, Viltres et al., 2020; Stamps et al., 2020) and red lines marking the Red Sea (RS), Gulf of Aden (GA) and Main Ethiopian Rift (MER) branches. The black dashed line in the inset marks the SW boundary of the Danakil Block (DB). D: Dabbahu, MH: Manda-Harraro, MI: Manda-Inakir, AG: Assal-Goubbeth, GoT: Gulf of Tadjoura. Small black circles show seismicity between 1950–2025 from the USGS National Earthquake Information Center. **(b)** Geological map depicting the volcanic products erupted in Afar since ∼ 20 Ma (modified after Tortelli et al., 2022; Rime et al., 2023). The values reported in **(b)** are rock ages from Courtillot et al. (1984), Kidane et al. (2003), Lahitte et al. (2003) and Feyissa et al. (2019). Areas covered by recent deposits are shown in white.

3.0–1.7 Ma (Daoud et al., 2011; Tortelli et al., 2022). Since the Stratoids emplacement, protracted rift localisation has resulted in the development of a series of en-echelon magmatic segments and tectonic grabens, which dominate the present-day topography (Fig. 1) (Barberi and Varet, 1977; Kidane et al., 2003; Lahitte et al., 2003; Ebinger et al., 2013). The first magmatic evidence of focused rifting dates to 1.1–0.6 Ma, with the eruption of the Gulf Basalts series more or less at the position of the modern magmatic segments and grabens (Stab et al., 2016). The present-day magmatic segments are 50–100 km long and resemble mid-ocean ridge segments, with extension being mainly accommodated by dike intrusions and faulting (Barberi and Varet, 1977; Hayward and Ebinger, 1996; Wright et al., 2012 Nobile et al., 2012; Pagli et al., 2012 Ruegg et al., 1979; Yirgu et al., 2006; Hamling et al., 2010).

In Central Afar, the modern magmatic segments are the Assal-Goubbeth (AG), Manda-Inakir (MI) and Dabbahu-Manda-Harraro (DMH) (Fig. 1a). The interaction between AG and MI occurs in the Makarassou area (Fig. 1) and is characterised by NNW-striking, low-angle normal faults

(Manighetti et al., 2001). To the west, the interaction between AG and DMH occurs across a ∼ 100 km wide area hosting the en-echelon grabens of Alol Der'Ela-Gaggade, Hanlé, Dobi, Immino and Tendaho-Goba'Ad (Fig. 1a) (e.g. Manighetti et al., 2001; Pagli et al., 2014; Doubre et al., 2017; Moore et al., 2021; Muluneh et al., 2024). These grabens are controlled by normal faults with throws >200 m, and the grabens are partially filled by Pleistocene-to-Recent deposits with varying thickness of 200–1000 m (Abbate et al., 1995). Among these grabens, Tendaho is suggested to have been a magmatic segment with fissural eruptions between ∼ 1.0–0.8 Ma (Fig. 1a), while minor activity after ∼ 0.2 Ma focused at the shield volcano Dama Ali (Acocella et al., 2008; Bridges et al., 2012; Ebinger et al., 2013; Tortelli et al., 2024). The current activity at the Central Afar grabens mainly consists of mechanical faulting with considerable seismicity (up to Mw ∼ 6.0) and of the emplacement of magmatic sills in the middle to lower crust (Hammond et al., 2011; Ruch et al., 2021; Ahmed et al., 2022; Rime et al., 2024; La Rosa et al., 2024).

In Southern Afar, the extension following the emplacement of the Lower Stratoids led to the development of the main Adda'Do graben at the axis of the rift and the Karrayyu graben further north-west (Varet, 2018; Rees et al., 2023). Adda'Do is ~ 100 km long, strikes NNE and is bounded on both sides by parallel half-graben structures. The graben has no evidence of eruptive fissures and is only dissected by the main central volcano Yangudi (Rees et al., 2023). Overall in Southern Afar, NNE-striking faults interact with a system of $\sim$ EW-striking faults, forming locally T-shaped architectures (Maestrelli et al., 2022, 2024). Intersecting structures, combined with recent observation of an EW-striking dike that intruded in 2001 (Keir et al., 2011), have been interpreted as being caused by two long-term co-acting extensional regimes related to the separation of Arabia and Somalia from Nubia (Maestrelli et al., 2024).

3   Method

In this study, we used an automatic fault extraction workflow implemented in the Fatbox software (Gayrin et al., 2025a). The methodology behind Fatbox is already provided in Gayrin et al. (2025b) and Wrona et al. (2023). Here we expanded the original package for DEM analysis by implementing new filters and by building up a novel workflow for the analysis of deformation components, such as the horizontal extension and the second invariant of strain (Figs. 2 and S1 in the Supplement). The method was applied to two DEM datasets to test the effectiveness of our approach at different spatial resolutions, (1) Copernicus GLO 90 m (Airbus, 2020) and (2) FABDEM V1-2 (Hawker et al., 2022), both covering an area of $\sim 108\,000$ km². The latter is a global elevation dataset obtained by filtering the contribution of buildings and trees from the Copernicus GLO 30 m DEM (Hawker et al., 2022). As a further validation, we also compared the results with those obtained from faults mapped manually in DMH.

3.1   Automatic fault extraction in Fatbox

Normal faults can induce sharp changes in the Earth's surface elevation due to relative vertical and horizontal motions between two crustal blocks. In the analysis of digital images, such as DEMs, these sharp gradients at adjacent pixels are referred to as *edges*. The basic rationale behind the fault extraction method in Fatbox is the detection of edges in the DEM and their subsequent conversion to a network called *graph* (Wrona et al., 2023; Gayrin et al., 2025a, 2025b). However, edges are not just related to faults but also to other geological elements, such as lava flows, volcanoes and river valleys, that introduce undesired artefacts. In this study, we thus adopted a modified version of the original Fatbox workflow presented in (Wrona et al., 2023) to face the new requirements of DEMs application and artefacts filtering in Afar.

A major difference between faults and other geological elements in a DEM is constituted by elevation changes and their spatial variability. In Afar for example, lava flows are characterised by lower-elevation changes and vary spatially over shorter length scales than faults. On this basis, we first applied an edge-preserving mean filter to highlight the long-range variability in the DEM, as that related to faults, while smoothing out the short-range noise caused by lava flows and other volcanic morphologies (e.g. scoria cones). This method calculates the mean of pixel values within a moving window, including just those whose absolute elevation difference exceeds a certain threshold value. For the 30 m DEM, a spatial window of 20 pixels and a threshold of 5 m allowed us to better emphasise fault scarps while smoothing surrounding noise (Fig. S1a and b).

Edge detection was performed on the filtered DEM using a Canny operator that tracks edges by hysteresis after applying an additional low-pass Gaussian filter (Fig. S1c). This is controlled by a kernel standard deviation (σ) along with two minimum and maximum gradient magnitude thresholds (Canny, 1986). These parameters are key as they influence the connection between adjacent features and affect the final fault number and segmentation. For the 30 m DEM, a Gaussian filter with σ equal to 3.5 and minimum/maximum thresholds of 1/14 was the best combination of parameters to remove artefacts but still maintain a robust fault segmentation. Additionally, small objects with size of 50 pixels and within a neighbourhood of 10 pixels were removed from the edge raster image, while bigger residual artefacts were removed after the graph generation.

A graph was generated after skeletonisation of the edges in the raster image (Wrona et al., 2023) (Figs. 2b and S1d). In the graph, each linear element representing a fault (or some undesired linear feature) is considered an individual component and identified by an individual number. Each component is made up of nodes and connecting lines (here referred to as *fault sections*), located in a Euclidean space (Fig. 2c). It follows that we can perform geometrical analyses of the graph components, and, by knowing the resolution and coordinates of the initial raster, we can translate them in either a metric or a geographic reference system.

We further developed a very effective filtering operation that is carried out at the graph level. A geometrical parameter that helps in distinguishing between faults and artefacts is the linearity (Λ), described as the ratio between tip to tip (l) and total length (L) of a linear feature. Faults are commonly characterised by a higher linearity than wavy artefacts (see Figs. S1 and Table S1 in the Supplement). However, this assumption is not always true: as can be seen in Table S1, small linear artefacts can exist and have higher linearity than longer curvilinear faults. To address this problem, we introduced a normalised scale-dependent linearity filter into Fatbox that considers the area covered by linear elements. Area-based methods have been shown to be more robust and less sensitive to noise, and various formulations of linearity with vary-
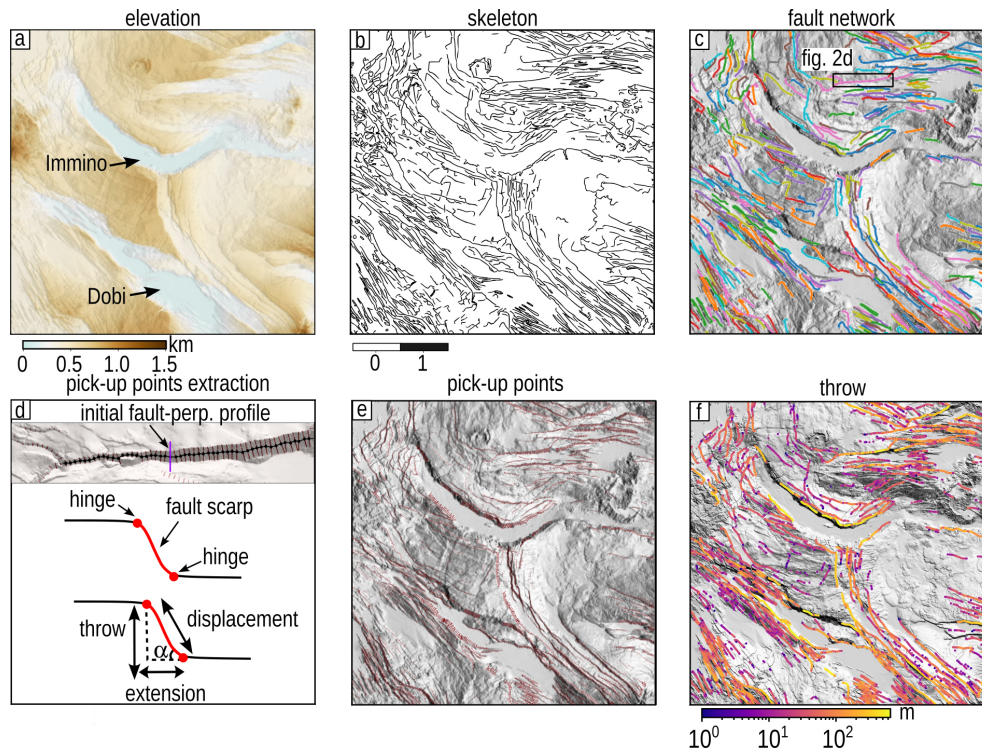
Figure 2. Main steps of the Fatbox workflow developed in this study. **(a)** Hillshade of the input DEM. **(b)** Skeletonised linear elements identified by the edge detector. **(c)** Filtered fault dataset converted to a graph. Colours here represent the fault identification number. **(d)** Basic sketch of the method for the fault scarp detection. **(e)** Pick-up points detected every 250 m along the fault scarp. **(f)** Final map of along-strike throw measurements at each fault. The FABDEM V1-2 DEM (Hawker et al., 2022) is used as the figure basis.

ing degrees of complexity have been proposed in the literature (e.g. Zunic and Rosin, 2011; Zunic et al., 2016). We therefore calculate a normalised scale-dependent linearity as

$$\Lambda_n = (l^2/L)/(L_{\max} - L_{\min}) \qquad (1)$$

with the denominator being the normalisation factor. Figure S1 and Table S1 show how this approach successfully under-weights the Λ_n values of small linear artefacts while over-weighting Λ_n values characterising longer curvilinear faults. The filtering is finally applied by simply removing all the graph components with Λ_n lower than a certain threshold.

3.2 Fault scarp quantification

The extraction of the fault scarp is performed by combining the graph and the original unfiltered DEM (Fig. 2d and e). For each fault section in the graph, Fatbox calculates the midpoint and draws an orthogonal profile by extending it to a given distance d, symmetrically toward the foot wall and the hanging wall. For each fault-orthogonal profile, the algorithm detects the two hinge points of the fault scarp (here referred to as pick-up points) by calculating the slope percentage at adjacent increments of the profile and stopping when its value reaches a given lower threshold (Fig. 2d and e). This

approach successfully isolates just the profile portion representative of the fault scarps and automatically adapts to the progressive tip-ward reduction of the fault throw, preventing the overlap of profiles pertaining to adjacent faults (Fig. 2d and e).

For each profile, the algorithm calculates the throw (Fig. 2e) and the horizontal extension (Ext_H) as the difference in the vertical and horizontal distances between the two pick-up points, respectively (Fig. 2d). These parameters are then used to calculate the dip angle (α) and the displacement along the fault scarp through simple trigonometric relationships. Fault-based measurements of Ext_H were used here to retrieve the magnitude of the strain tensor (more specifically the second invariant, $I2$). According to this aim, we first derived the EW and NS components of Ext_H as

$$\text{Ext}_{EW} = \text{Ext}_H \times \cos(\varphi) \qquad (2)$$
$$\text{Ext}_{NS} = \text{Ext}_H \times \sin(\varphi), \qquad (3)$$

where φ is the extension direction in radians, assuming an angle of $0°$ for the EW direction. We converted the pointwise measurements of Ext_{EW} and Ext_{NS} to a raster grid (Fig. S2). The bin size of the raster is a key parameter as it influences the number of measurements from adjacent faults falling within a pixel and the correspondence between pointwise and areal extension (Fig. S2). For our study, a bin size

of 300 m resulted in each pixel being representative of measurements of individual fault portions. To prevent averaging or summing effects caused by the presence of multiple segments pertaining to the same fault within the same pixel, we calculated the length-weighted components of extension (WExt$_{EW}$ and WExt$_{NS}$), corresponding to the sum of products between extension components and fault section lengths, divided by the total segment length within each pixel (Fig. S2). Figure S2 shows the agreement between the components of pointwise and areal extension. We refined our high-resolution dataset by manually masking pixels related to residual artefacts in the graph. The strain components ε_{EW} and ε_{NS} were then retrieved by dividing the components of extension for the pixel size. Finally, the second invariant of the strain tensor was calculated following Gerya (2019) as

$$I2 = \sqrt{1/2 \left(\varepsilon_{EW}^2 + \varepsilon_{NS}^2 \right)}. \tag{4}$$

We finally resampled our data to a ~ 3 km pixel size to ease the comparison between our dense fault-based $I2$ measurements and the regional (~ 15 km resolution) geodetic strain rates obtained by Muluneh et al. (2024). Resampling was performed by directional summation of the pixels in the high-resolution maps of the WExt$_{EW}$ and WExt$_{NS}$, followed by recalculation of the $I2$ at lower resolution (Fig. S3).

A DEM includes contributions to the elevation by deposits and lava flows, as those observed within the major grabens and magmatic segments in the study area. We therefore stress that our approach reconstructs only the most recent history of slip on a fault that ruptured the uppermost geological layers. Our $I2$ measurements can hence be considered to represent the minimum geological strain. In particular, considering the majority of faults rupturing the Upper and Lower Afar Stratoids formations, our maps mainly depict the distribution of strain during the last 4.5 Ma, the oldest age limit of the Lower Stratoids formation (Tortelli et al., 2022).

4 Results

4.1 Fault statistics

Our automatic fault extraction workflow allowed us to map 3917 and 2165 individual faults from the 30 m (Fig. 3) and 90 m (Fig. S4) DEMs, respectively. Fault-length distributions and average strikes in both datasets are presented in Figs. 3b c and S4. The datasets show similar fault orientations with a dominant NW-striking system, associated with a secondary system of $\sim$ SW-striking faults (Figs. 3b and S4b). The 30 m dataset consists of fault lengths ranging between ~ 0.8 and ~ 35 km, with the dominant class being 2.5–5.0 km, while the 90 m dataset is characterised by fault lengths between ~ 2.7 and ~ 45 km, dominated by 5–10 km long faults (Fig. 3c). The histograms in Fig. 3c show that the largest differences between the two datasets are observed

in length classes < 5 km, while longer faults are well represented in both datasets (Figs. 3a and S4a). This can be explained by the fact that the 90 m DEM has lower resolution and cannot capture shorter faults that are instead resolved by the 30 m DEM. Denser fault networks have been detected for example at Makarassou, north and west of Hanlé, as well as around Immino (Figs. 3, S3c and f, and S4). An additional explanation could be that at lower resolution, adjacent faults are identified as a single longer fault, which reduces the total number of faults in the dataset.

4.2 Data validation

Geological strains ($I2$) from the 30 and 90 m datasets show the same spatial distribution with strain maxima ranging between 0 and ~ 0.5 (Fig. S5). Spatially scattered residuals between the two datasets range ± 0.30 due to natural local differences at the scale of single pixels (Fig. S5c). While the two datasets are comparable, we based our observations and interpretation on the 30 m dataset as it provides higher detail and a larger number of faults. As a further, independent validation, we compared the results obtained from the 30 m DEM with those obtained from faults mapped manually. For this test, we mapped faults in the same sector of the DMH covered by the across strike profiles in Fig. 6 and calculated the associated strain (Fig. S6). We then isolated the faults and the associated strains covering the same area in the 30 m dataset. A comparison between the two datasets shows that they are characterised by similar strain values and spatial distribution (Fig. S6). Residuals between the manual and automatic datasets range ± 0.1, with just an outlier pixel giving a residual of 0.15. Assuming the manual dataset being representative of 100 % of the faults, we calculated that our automatic approach successfully retrieved 93.4 % of the total number of faults.

Finally, we explored the role of surface processes (e.g. erosion) and fault morphologies in lowering dip angles. In particular, we plotted the distribution of dip values in map view (Fig. S7a), along with the average fault dip angles as a function of fault throw (Fig. S7b). We found that for throws above 200 m, the average dip angles consistently range between 20–40° while the maximum dips reach $\sim 60°$ (Fig. S7a and b). These findings are similar to the dip angles measured in the field in various sectors of the rift (e.g. Makarassou, Geoffroy et al., 2014; west of Dabbahu, Stab et al., 2016) and with modelling of coseismic ruptures (e.g. La Rosa et al., 2019). However, we also found that smaller faults with throws less than 200 m have lower average dip angles and that their dip decreases with decreasing throw (Fig. S7b). Visual inspection of the DEM shows this is in part due to some erosion on the external (older) sectors of the rift and that most of the small offset faults are associated with a low-angle monocline caused by elastic flexure of rock above a propagating fault, as also observed by Hofmann et al. (2024) in DMH. We tested the effect of the low dip angle of the minor faults on the to-
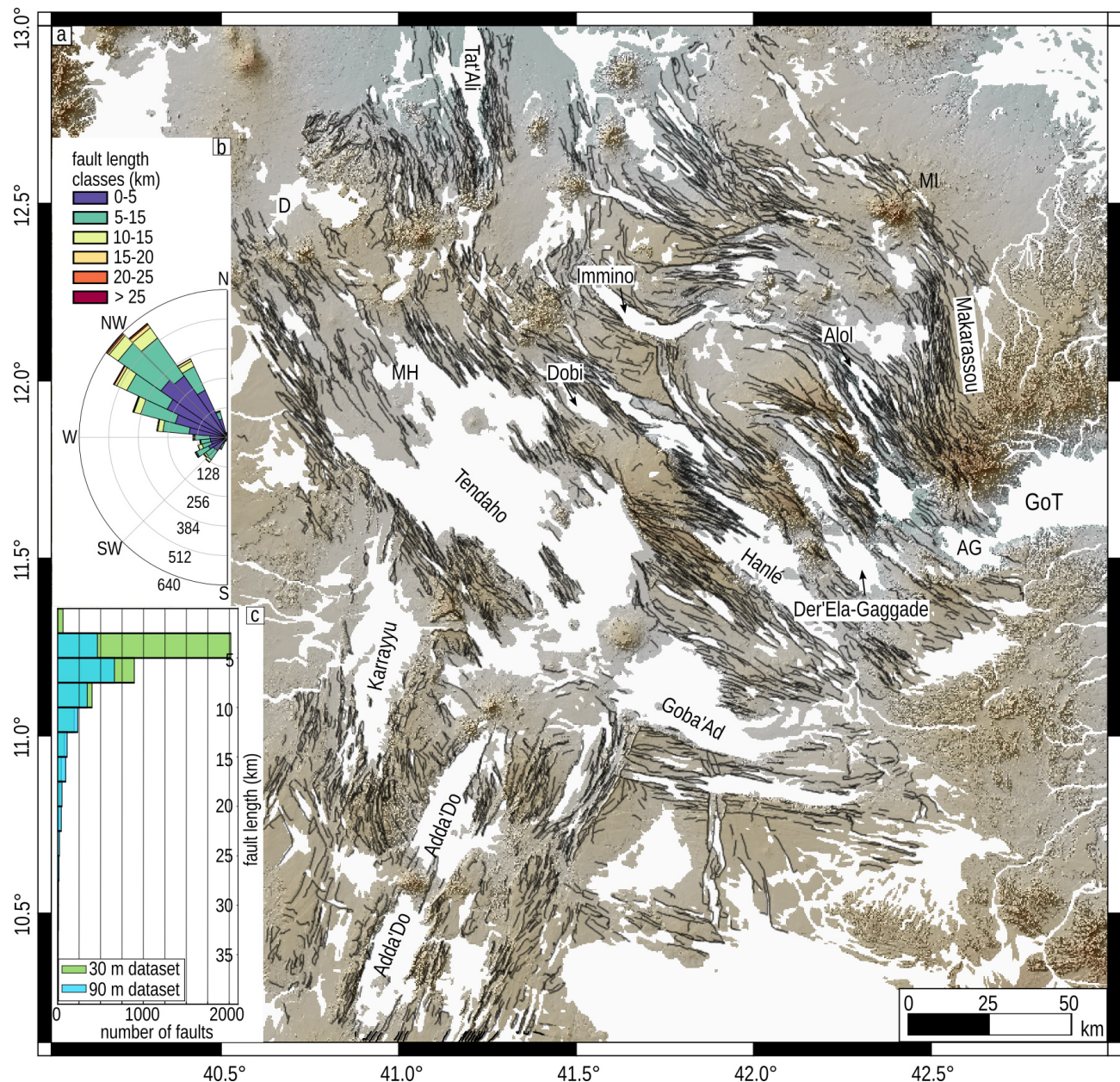
Figure 3. Results of the automatic fault extraction with Fatbox and statistical analysis. **(a)** Map of 3917 individual faults (black lines) extracted from the 30 m FABDEM. **(b)** Length-weighted rose diagrams of average fault strike distribution for the 30 m dataset. **(c)** Histograms comparing the fault-length distributions obtained with a 30 and a 90 m DEM. The histogram binning is 2.5 km. Names and abbreviations are the same as in Fig. 1. The FABDEM V1-2 DEM (Hawker et al., 2022) is used as the figure basis.

tal strain by employing a constant dip angle of 30° for those faults that feature throws lower than 200 m and dip angles lower than 20° (Fig. S7c, d and f). The results show that the spatial distribution of strain remains similar, with some decrease mainly observed on minor faults and in the external sectors of the rift (Fig. S7e and f). This implies that some overestimation of strain occurs where fault monoclines and debris are present, while the strain at the major grabens and axial magmatic segments is robustly deduced.

4.3 Spatial and temporal distribution of strain in Afar

In this section, we compare the results of the 30 m dataset with regional geodetic strain rates derived from InSAR and GPS during 2014–2021 (Muluneh et al., 2024; La Rosa et al., 2024) to address the link between short- and long-term deformation processes during rifting. We stress that our workflow provides the distribution of regional tectonic strain accommodated by faults over millions of years. The geodetic
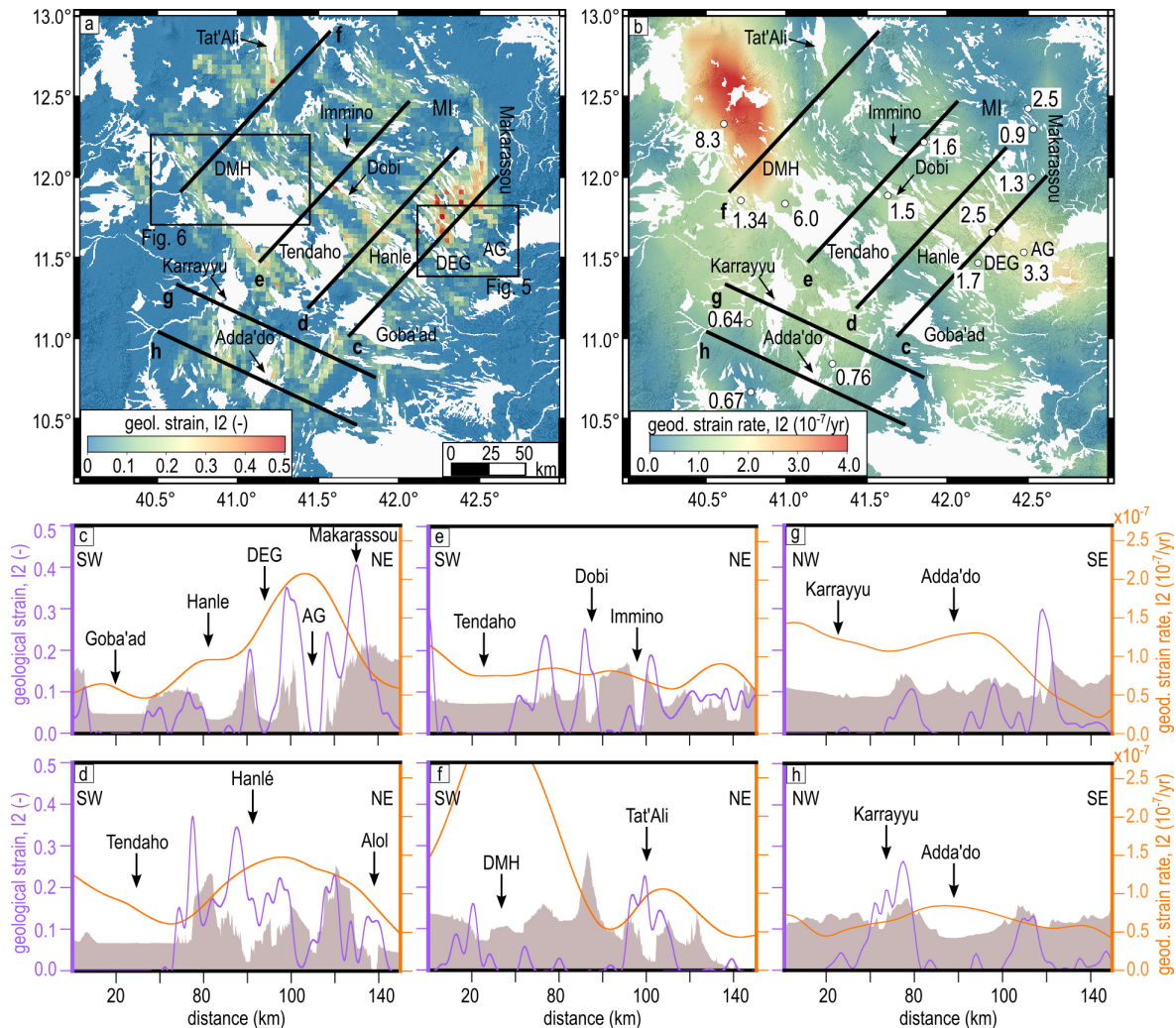
Figure 4. Results of our fault-based strain analysis and comparison with deformation rates from geodesy. **(a)** Map of the total geological strains (second invariant $I2$) at a 3 km resolution calculated from faults in Fig. 3a (30 m dataset). Note that our fault-based analysis derived geological strain that has been accumulated since ∼ 4.5 Myr in Southern Afar, and ∼ 2.5 Myr in Central Afar when previous faults have been covered in flood basalts of the Upper Stratoids Series. We saturated the colour bar for values above 0.5 to better highlight the strain variability. **(b)** Map of geodetic strain rates (second invariant) at 15 km resolution, modified after Muluneh et al. (2024). The FABDEM V1-2 DEM (Hawker et al., 2022) is used as the figure basis for panel **(a)** and **(b)**. Black lines are the profile tracks shown in **(c–h)**. The white dots and related numbers in **(b)** represent the calculated geological strain rates (in units of 10^{-7} yr^{-1}). **(c–h)** Large-scale profiles comparing geological strains (purple) and geodetic strain rates (orange). The brown filled profiles show the elevation obtained from the FABDEM V1-2 DEM (Hawker et al., 2022) for orientation (vertically exaggerated by a factor of 40).

strain on the other hand includes contributions from all deformation processes during rifting, such as magmatic activity, over decadal to annual time frames. Strain distributions are compared via a series of profiles crossing the most important tectonic and magmatic features in Central and Southern Afar, including the active magmatic segments and the major grabens (Figs. 4–6). We then converted geological strain to strain rates using rock dating and under the assumption of continuity of the rifting process (e.g. McClusky et al., 2010; Reilinger and McClusky, 2011), which provides lower bounds for the geological strain rates. The comparison was

possible only where well-constrained rock dating was available. Therefore, we used ages available close to the profiles and from rocks sampled at the top of the lava flows, avoiding older products at the base of fault scarps (Courtillot et al., 1984; Kidane et al., 2003; Lahitte et al., 2003; Feyissa et al., 2019, Tortelli et al., 2025). It was not possible to apply this approach to the entire strain map, but we selected enough data to cover the full range of possible ages across the whole rift. Differences between the geological strain rates calculated at different portions of the rift provide insights into the spatial migration of the rifting process with time, while dif-
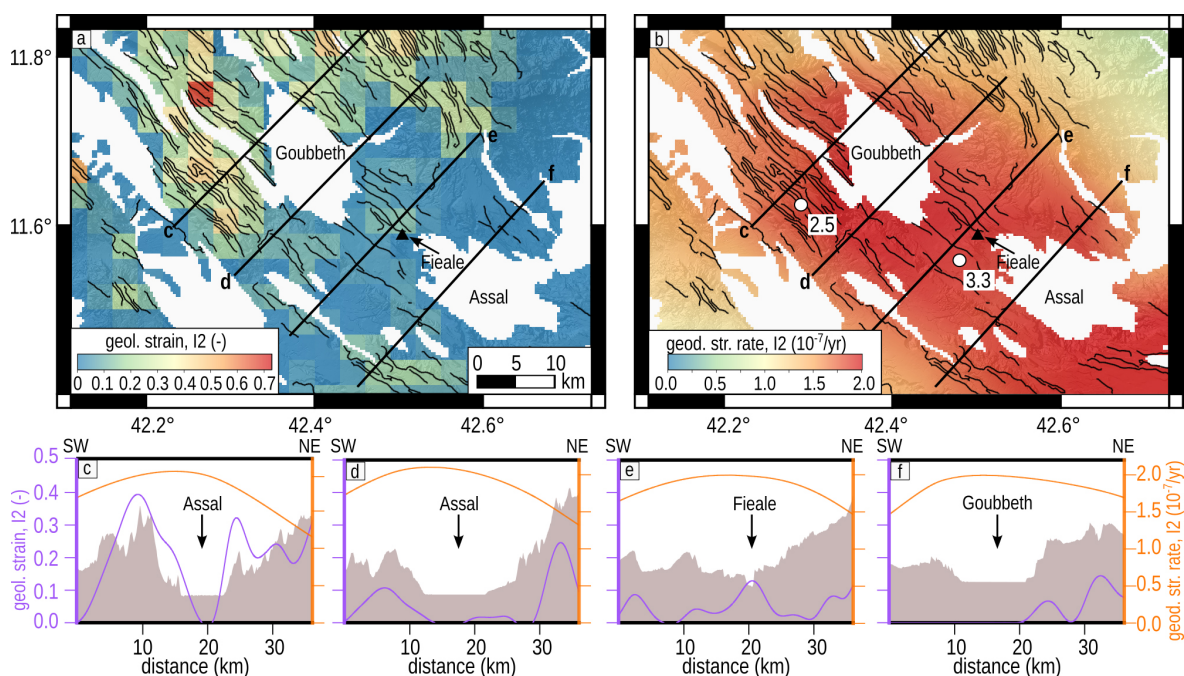
Figure 5. Details of strain distribution along the Assal-Goubbeth magmatic segment (see Fig. 4a for location). **(a)** Map of the total geological strains (second invariant) at 3 km resolution. Map of geodetic strain rates (second invariant, $I2$) at 15 km resolution, modified after Muluneh et al. (2024). Black curved lines depict faults as reported in Fig. 3a. Black straight lines designate profile tracks shown in **(c)–(f)**. Note that we modified and adapted the colour bars for a better visualisation of the strains in the area. The white dots and related numbers in **(b)** represent the calculated geological strain rates (in units of 10^{-7} yr^{-1}). **(c–f)** Detail profiles comparing geological strains (purple) and geodetic strain rates (orange). The brown filled profiles show the elevation (vertically exaggerated by a factor of ~ 13). The FABDEM V1-2 DEM (Hawker et al., 2022) is used as the figure basis.

ferences between measured geodetic and expected geological strain rates might suggest a possible role of magmatic processes in assisting extension. Note that the faults mapped in this study, and controlling the major tectonic grabens and magmatic segments, mainly developed in the Lower Stratoids in Southern Afar, and in the Upper Stratoids and the recent-most axial products in Central Afar (Ebinger et al., 2013; Tortelli et al., 2022; Rime et al., 2023). Our temporal reconstruction is thus limited to the last ~ 4.5 Myr in Southern Afar and the last ~ 2.5 Myr in Central Afar. Figure 4 shows the results at the rift scale, while Figs. 5 and 6 show details of the strain distribution at the scale of individual magmatic segments.

Geological strains ranging between 0.2 and 0.6 are observed at the AG magmatic segment, at the MI magmatic segment and in the Makarassou area (Figs. 1 and 4a, c). At Makarassou, geological strains are equal to 0.3 where the Upper Stratoids are dated to ~ 2.3 Ma, resulting in geological strain rates of $\sim 1.3 \times 10^{-7}$ yr^{-1}. These values are higher than geodetic measurements that show very low strain rates ($< 0.2 \times 10^{-7}$ yr^{-1}). At AG, strains are ~ 0.4 at the northern tip, along faults shaping the south-western margin of the Lake Assal graben (Figs. 4 and 5a, c). K/Ar dating of the top of the Upper Stratoids sampled in the area pro-

vides an age of ~ 1.6 Ma (Courtillot et al., 1984), which results in a long-term strain rate of $\sim 2.5 \times 10^{-7}$ yr^{-1}, notably similar to the geodetic strains currently accumulating there. The axial sector of AG is represented by the Fieale area, the locus of recent-most lava flows and the 1978 rifting episode. Here, faults developing above 0.15 Ma old volcanic products accommodated geological strains of ~ 0.05, corresponding to strain rates of $\sim 3.3 \times 10^{-7}$ yr^{-1} (Fig. 5d). Geodesy in this area measured strain accumulating at a rate of $\sim 2.0 \times 10^{-7}$ yr^{-1} (Muluneh et al., 2024; La Rosa et al., 2024). In MI, geological strains of 0.22 are measured on faults cutting the Upper Stratoids (~ 2.4 Ma), resulting in geological strain rates of 0.9×10^{-7} yr^{-1}. Conversely, faults forming on more recent axial products (~ 0.6 Ma) accommodated geological strains of 0.15, equivalent to a strain rate of 2.5×10^{-7} yr^{-1}, which is the same as those measured at the axis of AG. However, current geodetic strain rates are significantly lower and equal to $\sim 0.2 \times 10^{-7}$ yr^{-1}.

Geological strains of 0.05–0.2 are reached along the DMH magmatic segments, the locus of the 2005–2010 rifting episode (Fig. 4a and f). At DMH, geological strains range from ~ 0.2 at margins to ~ 0.05 at the segment axis (Figs. 4a, f and 6). In particular, values of ~ 0.17 are measured on the south-western margin of Manda-Harraro, along
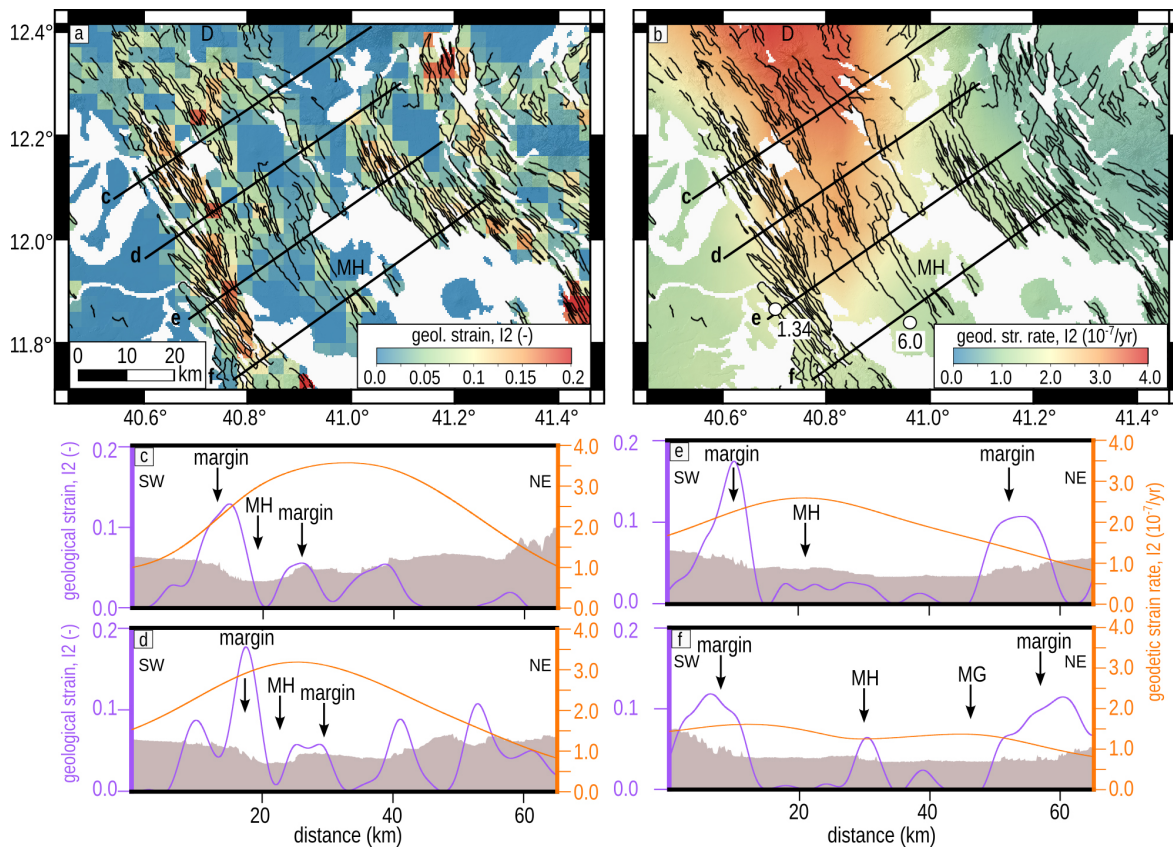
Figure 6. Details of strain distribution along the Manda-Harraro (MH) magmatic segment (see Fig. 4a for location). **(a)** Map of the total geological strains (second invariant, $I2$) at 3 km resolution. Map of geodetic strain rates (second invariant) at 15 km resolution, modified after Muluneh et al. (2024). Black curved lines are the faults as reported in Fig. 3a, while the black straight lines are the profile tracks shown in **(c)**–**(f)**. Note that we modified and adapted the colour bars for a better visualisation of the strains in the area. The white dots and related numbers in **(b)** are the calculated geological strain rates (in units of 10^{-7} yr^{-1}). D = Dabbahu. **(c–f)** Detail profiles comparing geological strains (purple) and geodetic strain rates (orange). The brown filled profiles show the elevation (vertically exaggerated by a factor of ~ 7). The FABDEM V1-2 DEM (Hawker et al., 2022) is used as the figure basis.

faults cutting the Upper Stratoids (Fig. 6). K/Ar dating in the same area gives an Upper Stratoids age of 1.2 Ma (Lahitte et al., 2003), which results in a geological strain rate of $\sim 1.34 \times 10^{-7}$ yr^{-1} (Fig. 6). The inner sector of Manda-Harraro shows strains of ~ 0.08–0.06 where axial products have ages of ~ 0.12–0.04 Ma (Lahitte et al., 2003). These values correspond to geological strain rates ranging from 6.0×10^{-7} to 1.5×10^{-7} yr^{-1}, higher than those measured at the margins and comparable to the geodetic strain rates currently accumulating in the same area (Figs. 4b, f and 6). At Dabbahu, geological strains equal to 0.02 have been measured on faults cutting the recent volcanic products (0.024 Ma). This finding demonstrates that Dabbahu exhibits the highest geological strain rates in Central Afar, with values of 8.3×10^{-7} yr^{-1}. The same area shows the highest current geodetic strain rates ($>3.5 \times 10^{-7}$ yr^{-1}). Finally, geological strains up to 0.4 are accommodated by faults shaping the southern tip of TA (Fig. 4a and f), where geodetic strain rates are still on the order of $\sim 1.0 \times 10^{-7}$ yr^{-1} (Fig. 4f).

Between AG and DMH, plate divergence and interaction between the two magmatic segments occur across a ~ 100 km wide area of distributed extension hosting the major en-echelon grabens of Der'Ela-Gaggade, Hanlé, Tendaho, Goba'Ad, Dobi and Immino (Fig. 4a, d, and e) (Manighetti et al., 2001; Ruch et al., 2021; Rime et al., 2023; Muluneh et al., 2024). Here, the Upper Stratoids get progressively younger toward the north-west. Average ages of ~ 2.0 Ma are measured between Der'Ela-Gaggade and Hanlé (Courtillot et al., 1984) where the highest geological strains amount to ~ 0.35 (Fig. 4e). Ages of ~ 1.7 Ma have been found between Tendaho and Dobi (Kidane et al., 2003; Feyissa et al., 2019) where the highest geological strain is ~ 0.25 (Fig. 4d). Finally, the ~ 1.5 Ma ages deduced at Immino (Lahitte et al., 2003) correspond to maximum geological strains of ~ 0.24. These total strains and ages give approximately constant geological strain rates across the area, with values of $\sim 1.7 \times 10^{-7}$ yr^{-1} between Der'Ela-Gaggade and Hanlé, $\sim 1.5 \times 10^{-7}$ yr^{-1} between

Tendaho and Dobi, and $\sim 1.6 \times 10^{-7}$ yr^{-1} at Immino. However, these grabens host thick deposits (200–1000 m, Abbate et al., 1995) that hide part of the fault scarps. This implies that the major graben-bounding faults actually accommodated higher strains during geological times. Profiles Fig. 4d and e show current geodetic strains cumulating at rates of $\sim 1.5 \times 10^{-7}$ yr^{-1}. Assuming an underestimation of geological strains rates in the area, current geodetic strain rates are thus lower than the long-term ones.

In Southern Afar, geological strains up to ~ 0.30 are accommodated at the Adda'Do graben and along a series of parallel half-graben structures (Fig. 4a, g and h). EW-striking faults also accommodated strains up to ~ 0.17, shaping the north-eastern boundary with the Central Afar and the internal sectors of Southern Afar. West of Adda'Do, the Karrayyu graben shows strains ranging from ~ 0.30 at the southern tip to ~ 0.16 at the northern termination (Fig. 4a and g). The Lower Stratoids in Southern Afar vary in age from an average of ~ 4.5 Ma between the western margin of Adda'Do and the southern tip of Karrayyu (Lahitte et al., 2003; Feyissa et al., 2019) to ~ 2.5 Ma west of Karrayyu (Feyissa et al., 2019) (Fig. 1b). These values provide almost constant geological strain rates of 0.67×10^{-7} yr^{-1} and 0.64×10^{-7} yr^{-1}. Geodetic data instead show a northward increase in current strain rates from $\sim 0.2 \times 10^{-7}$ to $\sim 1.1 \times 10^{-7}$ yr^{-1}, with strains accumulating equally at both Adda'Do and Karrayyu. Strains are also accumulating at rates of $\sim 1.1 \times 10^{-7}$ yr^{-1} along the north-eastern border of Southern Afar.

5 Discussion

We analysed the spatial and temporal variations of deformation in the Central and Southern sectors of the Afar rift using a method for the calculation of long-term geological strains from automatically mapped faults and by combining these observations with current geodetic strain rates and rock dating. This automatic approach was tested on DEMs at various resolutions and validated with manually mapped faults. Our method successfully isolated most of the faults in the study area, minimising artefacts introduced by other morphologies in the DEMs. We show that our results are independent of the DEM resolution as strains obtained from both the 30 m and the 90 m datasets are comparable with major regional faults being equally represented and different fault systems being likewise well resolved. Some natural differences in the number of faults were observed due to the different levels of detail and fault segmentation dependent on the DEMs resolution. Other minor differences in the final strain maps are also introduced during raster resampling, yet this parameter can be changed easily and adapted for analyses at different spatial scales. For our purposes, the 30 m DEM and a map resampling at 3 km provided the best result in terms of the number of faults detected, level of detail and similarity with independent geodetic data. A comparison with manual map-

ping in the key area of DMH shows that our approach can resolve 93.4 % of the total strain in a study area, lending further robustness to our automatic fault extraction techniques. In conjunction with an independent prior study (Wrona et al., 2023), we conclude that Fatbox can be successfully applied to extract faults and quantify along-strike geometries from different types of data. Further applications of these methods could be used to analyse analogue and numerical models that are comparable to larger-scale DEMs. However, we also underline that some limitations in our method remain. Our approach works best in extensional tectonic settings (such as the Afar rift) where faults are active and/or characterised by sharp edges in the topography. Furthermore, our method cannot resolve the strike-slip component of faults as this motion does not generate any measurable vertical throw in a DEM. Further developments of Fatbox might account for the analysis of optical imagery or the automatic detection and measurement of lateral geomorphological offset (e.g. rivers) or other displaced objects (e.g. edges of lava flows).

The fault distribution and the analysis of geological and geodetic strains combined with dated rocks shed light on the long-term tectonic evolution of different sectors of the Afar rift, including individual magmatic segments and their interaction zones. At the regional scale, the major fault systems and the highest strains were measured in Central Afar (Figs. 3 and 4) characterised by faster divergence velocities (up to ~ 20 mm yr^{-1}) compared to the Southern Afar, during the last ~ 2.5 Myr (e.g. Doubre et al., 2017; Viltres et al., 2020). The Central Afar is characterised by a dominant system of NW-striking normal faults, mainly developing along the current regional axis of the rift systems, and a secondary system of NNW-striking faults observed at external sectors (e.g. in Makarassou). Faults at the external sectors of the rift show geological strains comparable to those measured at the current axis (e.g. Fig. 4a and c), indicating they accommodated large extension in the past, but they are currently accumulating very low strain rates. Similarly, relatively high geological strains were accommodated in MI at least until ~ 0.6 Ma. The segment experienced more recent volcanic eruptions but is currently characterised by geodetic strain rates close to zero and lack of seismicity (Muluneh et al., 2024; La Rosa et al., 2024). At the current rift axis, the faults that shape the active magmatic segments and the major grabens in Central Afar cut the Upper Stratoids and the younger axial products. The faults on the Stratoids show a progressive decrease of geological strains (and inferred strain rates) from south-east around AG to north-west around DMH. Our strain measurements in AG agree with the relative high strains previously measured in the same area by Polun et al. (2018), yet some discrepancies are observed elsewhere in MI and Makarassou. These differences might be partially caused by the different spatial resolutions characterising the two studies. Our observations are consistent with modern reconstructions of Afar evolution, whereby the opening of Central/Northern Afar was accompanied by the anti-clockwise

rotation of the Danakil block and the progressive focusing of extension and magmatic activity to the axis since ~ 1.1 Ma (e.g. Eagles et al., 2002; McClusky et al., 2010; Ebinger et al., 2013; Viltres et al., 2020; Rime et al., 2023). In this scenario, the larger geological strain rates at AG compared to DMH agree with faster velocities at the southern termination of the Danakil block (McClusky et al., 2010; Viltres et al., 2020). The Makarassou area and the MI segment currently do not accommodate significant extension, compatible with migration of the extension and magmatic activity toward the current rift axis represented by AG and DMH. MI has shown high geological strain at least since ~ 0.6 Ma, indicating a decrease in activity sometime after this period. However, the lack of overlap between more recent rock ages and geological strain measurements prevents us from obtaining an accurate estimation of the timing of this reduction. Furthermore, larger total strains in the south-eastern sector, combined with the observation of progressive younger Stratoids toward the north-west, point toward a long-term evolution of Central Afar characterised by a northward propagation of the rifting process, as already hypothesised by Lahitte et al. (2003) and Rime et al. (2023). Our results are also in agreement with the most recent models of asymmetric north-westward localisation of rifting proposed by Tortelli et al. (2025) on the bases of new geochemical analyses and Ar–Ar dating in Central Afar.

Both AG and DMH magmatic segments show a strong increase in strain rates at inner sectors compared to the margins. At the inner sectors we measured strains in the ~ 0.12 Ma old axial products, yet the first phases of axial magmatism are represented by the older and sparse Gulf series (~ 0.6 Ma). In AG, geological and geodetic strain rates are highest in Fieale. Here, strains accommodated by dike intrusions and faulting during the rifting episode of 1978 were 3 orders of magnitude higher than those currently accumulating (Tarantola et al., 1979). Opening velocities were still 3–4 times larger than average plate divergence rates during the ~ 8 years following the intrusion (Ruegg et al., 1984), with an accelerated post-rifting phase likely lasting until 2001 (Doubre et al., 2007). Geodesy shows that the ongoing inter-rifting strains are the results of a combination of tectonic and magmatic processes beneath AG (Muluneh et al., 2024; La Rosa et al., 2024). DMH shares similar features, with increased geological and geodetic strain rates at the inner portion of the magmatic segment. This area accommodated strain of the order of 10^{-5} during the co-rifting episode of 2005–2010 (Grandin et al., 2010). The rifting episode was characterised by 13 dike intrusions with associated faulting, and by increased fault slip rates due to further magma motions during inter-diking phases (Grandin et al., 2010; Dumont et al., 2016; Hamling et al., 2010; Wright et al., 2012; Pagli et al., 2014). Recent geodetic surveys also showed that DMH is currently experiencing a post-rifting phase accompanied by renewed magma inflow and inflation (Moore et al., 2021). The presence of a long-lived magmatic sys-

tem at the AG and DMH magmatic segments is widely testified by surface evidence of volcano-tectonic activity (Dumont et al., 2017), geochemical reconstructions (Medynski et al., 2015; Tortelli et al., 2024) and geophysical observations (e.g. Doubre and Peltzer, 2007; Keir et al., 2009; Wright et al., 2012; Smittarello et al., 2016). The increase in strain rates from the margin to the intruded inner portion of the magmatic segments during geological times, together with the decadal scale increase in geodetic strain rates during diking episodes, suggests that magmatism is an important long-term process promoting strain. Numerical models of magma intrusions in the shallow crust show that the increased heat flow and thermal gradients weaken the crust surrounding magma bodies and induce thermo-mechanical heterogeneities that promote strain focusing, increased strain rates and fault slip (e.g. Regenauer-Lieb et al., 2008; Douglas et al., 2016; Dumont et al., 2017; Brune et al., 2023). Shallow faulting is also promoted mechanically by dikes as dilation induces tensile forces at the upper tips of the intrusion (e.g. Trippanera et al., 2015). The long-term increase in the strain rates at the inner portion of the magmatic segments during at least the last 0.12 Myr might thus have two and possibly concomitant causes. On the one hand, the faults that we mapped might be the surface expression of past rifting (or single diking) episodes that released large strains in narrow zones during short time spans. On the other hand, the presence of long-lived shallow magmatic systems might have promoted a long-term increase in the fault slip rate in a weakened crust.

A ~ 100 km^2 wide area of distributed faulting accommodates the extension between AG and DMH magmatic segments. In this area, most of the strain focuses at Der'Ela-Gaggade, Hanlé, Tendaho, Goba'Ad, Dobi and Immino grabens (Fig. 4a, b, d, and e). Here, a thick deposit cover (1000–1600 m, Abbate et al., 1995) reduces our fault-based measurements, but including the vertical extent of the accommodation space in the throw calculation provides strains comparable to those accommodated at the adjacent magmatic segments. Geodesy shows instead that current strain rates are accumulating at rates lower than the magmatic segments. A possible explanation could be that some of these grabens grew by a combination of faulting and dike intrusion in the past, as shown by the presence of axial products and volcanic centres in the southern Tendaho graben (Fig. 1). Current seismic imaging, geodetic modelling and crustal balance calculations instead show the presence of a lower crust heavily intruded by mafic rocks that constitute up to the 40 % of the total volume (e.g. Hammond et al., 2011; Ahmed et al., 2022; Rime et al., 2024; La Rosa et al., 2024). Therefore, diffuse and protracted magma addition into the lower crust likely contributes to extension and reduces fault-related extension (Rime et al., 2024).

In Southern Afar, SSW-striking fault systems accommodate most of the geological strains induced by the ESE-directed separation of the Somalian plate from Nubia. Ge-

ological strain rates are uniformly distributed and generally lower than those measured in Central Afar. This is not unexpected considering the low-divergence velocities characterising Southern Afar (Birhanu et al., 2016; Doubre et al., 2017). Lower strain rates were also accommodated by systems of EW-striking faults that formed at the north-eastern boundary with Central Afar and within the internal sectors of Southern Afar (Fig. 4). These structures, along with the opening of an EW-striking dike in 2001 (Keir et al., 2011), have been recently suggested to be the evidence of two NE-directed and EW-directed co-acting extensional regimes in the area (Maestrelli et al., 2024). Our geodetic observations of strain rates accumulating along both EW-striking and SSW-striking faults support this hypothesis and indicate that Southern Afar is currently experiencing the superposing effects of the separation of both Arabia and Somalia from Nubia.

6 Conclusion

In this study we developed an automatic approach for the accurate identification of faults in DEMs and the calculation of geometrical parameters, slip components and horizontal strains. Our method was tested at various DEM resolutions, and the data were validated by comparison with those obtained on manually mapped faults, yielding overall similar results. We applied our method on the central and southern sectors of the Afar rift, where we combined fault-based measurements with geodesy and rock dating to reconstruct the long-term distribution of strain and its relationship with the tectonic and magmatic evolution of the rifting process. Our main results can be summarised as follows:

1. During the last ~ 2.5 Ma, the rifting process in Central Afar has propagated toward the NNW from AG to DMH, as suggested by higher total strain in the southeastern sector and by the Stratoids ages getting younger in the same direction.

2. During the last 0.6 Ma, the external sectors of the Afar rift, including Makarassou and MI, have not been the main locus of strain following the migration and focusing of extension to the rift axis.

3. At the magmatic segments, strains in the inner sectors are higher than those accommodated at the margins, likely due to magmatic activity that promotes dike-assisted extension and associated faulting. Diking also weakens crustal rheology that increases the strain rates.

4. AG and DMH interact across a ~ 100 km wide area where spatially constant strains, as high as those accommodated at AG, were uniformly accommodated during the last 2.5 Ma by a series of en-echelon grabens.

5. During the last 4.5 Myr, Southern Afar has experienced a bi-directional extension induced by the separation of both Somalia and Arabia from Nubia.

6. Strain in Southern Afar is accommodated not just at the axis but also by lateral graben structures, such as Karrayyu.

References

Abbate, E., Passerini, P., and Zan, L.: Strike-slip faults in a rift area: a transect in the Afar Triangle, East Africa, Tectonophysics, 241, 67–97, https://doi.org/10.1016/0040-1951(94)00136-W, 1995.

Acocella, V., Abebe, B., Korme, T., and Barberi, F.: Structure of Tendaho Graben and Manda Hararo Rift: Implications for the evolution of the southern Red Sea propagator in Central Afar, Tectonics, 27, 1–17, https://doi.org/10.1029/2007TC002236, 2008.

Ahmed, A., Doubre, C., Leroy, S., Keir, D., Pagli, C., Hammond, J. O. S., Ayele, A., Be de Berc, M., Grunberg, M., Vergne, J., Pestourie, R., Mamo, D., Kibret, B., Cubas, N., Lavayssière, A., Janowski, M., Lengliné, O., La Rosa, A., Chambers, E. L., and Illsley-Kemp, F.: Across and along-strike crustal structure variations of the western Afar margin and adjacent plateau: Insights from receiver functions analysis, J. African Earth Sci., 192, 104570, https://doi.org/10.1016/j.jafrearsci.2022.104570, 2022.

Airbus Defence and Space: Copernicus DEM GLO-90, Copernicus Data Space Ecosystem [data set], https://doi.org/10.5270/ESA-c5d3d65, 2020.

Barberi, F. and Varet, J.: Volcanism of Afar: Small-scale plate tectonics implications, GSA Bull., 88, 1251–1266, https://doi.org/10.1130/0016-7606(1977)88<1251:VOASPT>2.0.CO;2, 1977.

Biggs, J., Amelung, F., Gourmelen, N., Dixon, T. H., and Kim, S.: InSAR observations of 2007 Tanzania rifting episode reveal mixed fault and dyke extension in an immature continental rift, Geophys. J. Int., 179, 549–558, https://doi.org/10.1111/j.1365-246X.2009.04262.x, 2009.

Birhanu, Y., Bendick, R., Fisseha, S., Lewi, E., Floyd, M., King, R., and Reilinger, R.: GPS constraints on broad scale extension in the Ethiopian Highlands and Main Ethiopian Rift, Geophys. Res. Lett., 43, 6844–6851, https://doi.org/10.1002/2016GL069890, 2016.

Boone, S. C., Balestrieri, M., and Kohn, B.: Tectono-Thermal Evolution of the Red Sea Rift, Front. Earth Sci., 9, 1–9, https://doi.org/10.3389/feart.2021.713448, 2021.

Bridges, D. L., Mickus, K., Gao, S. S., Abdelsalam, M. G., and Alemu, A.: Magnetic stripes of a transitional continental rift in Afar, Geology, 40, 203–206, https://doi.org/10.1130/G32697.1, 2012.

Brune, S., Kolawole, F., Olive, J., Stamps, D. S., Buck, W. R., Buiter, S. J. H., Furman, T., and Shillington, D. J.: Geodynamics of continental rift initiation and evolution, Nat. Rev. Earth Environ., 4, 235–253, https://doi.org/10.1038/s43017-023-00391-3, 2023.

Calais, E., D'Oreye, N., Albaric, J., Deschamps, A., Delvaux, D., Déverchère, J., Ebinger, C., Ferdinand, R. W., K., F., Mcheyeki, A. S., Oyen, A., Perrot, J., Saria, E., Smets, B., Stamps, D. S., and Wauthier, C.: Strain accommodation by slow slip and dyking in a youthful continental rift, East Africa, Nature, 456, 783–788, https://doi.org/10.1038/nature07478, 2008.

Canny, J.: A Computational Approach to Edge Detection, IEEE Trans. Pattern Anal. Mach. Intell., PAMI-8, 679–698, https://doi.org/10.1109/TPAMI.1986.4767851, 1986.

Corti, G., Cioni, R., Franceschini, Z., Sani, F., Scaillet, S., Molin, P., Isola, I., Mazzarini, F., Brune, S., Keir, D., Erbello, A., Muluneh, A. A., Illsley-Kemp, F., and Glerum, A.: Aborted propagation of the Ethiopian rift caused by linkage with the Kenyan rift, Nat. Commun., 10, 1309, https://doi.org/10.1038/s41467-019-09335-2, 2019.

Courtillot, V., Achache, J., Landre, F., Bonhommet, N., Montigny, R., and Féraud, G.: Episodic spreading and rift propagation: New paleomagnetic and geochronologic data from the Afar Nascent passive margin, J. Geophys. Res., 89, 3315–3333, https://doi.org/10.1029/JB089iB05p03315, 1984.

Daoud, M. A., Gall, B. Le, Maury, R. C., Rolet, J., and Huchon, P.: Young rift kinematics in the Tadjoura rift, western Gulf of Aden, Republic of Djibouti, Tectonics, 30, https://doi.org/10.1029/2009TC002614, 2011.

Doubre, C. and Peltzer, G.: Fluid-controlled faulting process in the Asal Rift, Djibouti, from 8 yr of radar interferometry observations, Geology, 35, 69–72, https://doi.org/10.1130/G23022A.1, 2007.

Doubre, C., Manighetti, I., Dorbath, L., Dorbath, C., Bertil, D., and Delmond, J. C.: Crustal structure and magmato-tectonic processes in an active rift (Asal-Ghoubbet, Afar, East Africa): 2. Insights from the 23-year recording of seismicity since the last rifting event, J. Geophys. Res., 112, 1–32, https://doi.org/10.1029/2006JB004333, 2007.

Doubre, C., Déprez, A., Masson, F., Socquet, A., Lewi, E., Grandin, R., Nercessian, A., Ulrich, P., De Chabalier, J., Saad, I., Abayazid, A., Peltzer, G., Delorme, A., Calais, E., and Wright, T.: Current deformation in Central Afar and triple junction kinematics deduced from GPS and InSAR measurements, Geophys. J. Int., 208, 936–953, https://doi.org/10.1093/gji/ggw434, 2017.

Douglas, M. M., Geyer, A., Álvarez-valero, A. M., and Martí, J.: Modeling magmatic accumulations in the upper crust: Metamorphic implications for the coun-

try rock, J. Volcanol. Geotherm. Res., 319, 78–92, https://doi.org/10.1016/j.jvolgeores.2016.03.008, 2016.

Dumont, S., Socquet, A., Grandin, R., Doubre, C., and Klinger, Y.: Surface displacements on faults triggered by slow magma transfers between dyke injections in the 2005-2010 rifting episode at Dabbahu-Manda-Hararo rift (Afar, Ethiopia), Geophys. J. Int., 204, 399–417, https://doi.org/10.1093/gji/ggv449, 2016.

Dumont, S., Klinger, Y., Socquet, A., Doubre, C., and Jacques, E.: Magma influence on propagation of normal faults: Evidence from cumulative slip profiles along Dabbahu-Manda-Hararo rift segment, J. Struct. Geol., 95, 48–59, https://doi.org/10.1016/j.jsg.2016.12.008, 2017.

Eagles, G., Gloaguen, R., and Ebinger, C.: Kinematics of the Danakil microplate, Earth Planet. Sc. Lett., 203, 607–620, https://doi.org/10.1016/S0012-821X(02)00916-0, 2002.

Ebinger, C., Ayele, A., Keir, D., Rowland, J., Yirgu, G., Wright, T., Belachew, M., and Hamling, I.: Length and Timescales of Rift Faulting and Magma Intrusion: The Afar Rifting Cycle from 2005 to Present, Annu. Rev. Earth Planet. Sci., 38, 439–466, https://doi.org/10.1146/annurev-earth-040809-152333, 2010.

Ebinger, C. J., van Wijk, J., and Keir, D.: The time scales of continental rifting: Implications for global processes, Geol. Soc. Am., 2500, 1–26, https://doi.org/10.1130/2013.2500(11), 2013.

Ebinger, C., van Wijk, J., Olaka, L., Mériaux C., and Fontijn, K.: All scales must be considered to understand rifts, Nat. Rev. Earth Environ., 4, 209–210, https://doi.org/10.1038/s43017-023-00408-x, 2023.

Feyissa, D. H., Kitagawa, H., Bizuneh, T. D., Tanaka, R., Kabeto, K., and Nakamura, E.: Transition from Plume-driven to Plate-driven Magmatism in the Evolution of the Main Ethiopian Rift, J. Petrol., 60, 1681–1715, https://doi.org/10.1093/petrology/egz043, 2019.

Gayrin, P., Wrona, T., and Brune, S.: Fatbox, the fault analysis toolbox (1.1), GFZ Helmholtz Centre for Geosciences, GitHub [code], https://github.com/PaulineGayrin/Fatbox, 2025a.

Gayrin, P., Wrona, T., Brune, S., Neuharth, D., Molnar, N., La Rosa, A., and Naliboff, J.: Fatbox: the fault analysis toolbox, EGUsphere [preprint], https://doi.org/10.5194/egusphere-2025-3989, 2025b.

Geoffroy, L., Le Gall, B., Daoud, M. A., Jalludin, M.: Flip-flop detachment tectonics at nascent passive margins in SE Afar, Journal of the Geological Society, 171, 689–694, https://doi.org/10.1144/jgs2013-135, 2014.

Gerya, T.: Introduction to Numerical Geodynamic Modelling, 2nd edn., Cambridge University Press, https://doi.org/10.1017/9781316534243, 2019.

Gianpietro, T., Dominguez, S., and Malavieielle, J.: Automatic Fault Mapping in Remote Optical Images and Topographic Data With Deep Learning, J. Geophys. Res.-Sol. Ea., 126, 1–38, https://doi.org/10.1029/2020JB021269, 2021.

Grandin, R., Socquet, A., Jacques, E., Mazzoni, N., de Chabalier, J., and King, G. C. P.: Sequence of rifting in Afar, Manda-Hararo rift, Ethiopia, 2005–2009: Time-space evolution and interactions between dikes from interferometric synthetic aperture radar and static stress change modeling, J. Geophys. Res.-Sol. Ea., 115, 2156–2202, https://doi.org/10.1029/2009JB000815, 2010.

Hamling, I. J., Wright, T. J., Calais, E., Bennati, L., and Lewi, E.: Stress transfer between thirteen successive dyke intrusions in Ethiopia, Nat. Geosci., 3, 713–717, https://doi.org/10.1038/ngeo967, 2010.

Hammond, J. O. S., Kendall, J. M., Stuart, G. W., Keir, D., Ebinger, C., Ayele, A., and Belachew, M.: The nature of the crust beneath the Afar triple junction: Evidence from receiver functions, Geochem. Geophy. Geosy., 12, https://doi.org/10.1029/2011GC003738, 2011.

Hawker, L., Uhe, P., Paulo, L., Sosa, J., Savage, J., Sampson, C., and Neal, J.: A 30 m global map of elevation with forests and buildings removed, Environmental Res. Lett., 17, https://doi.org/10.1088/1748-9326/ac4d4f, 2022.

Hayward, N. J. and Ebinger, C. J.: Variations in the along-axis segmentation of the Afar Rift system, Tectonics, 15, 244–257, 1996.

Hofmann, B., Magee, C., Wright, T.: Throw distribution across the Dabbahu–Manda Hararo dike-induced fault array: Implications for rifting and faulting, Geology, 53, 161–165, https://doi.org/10.1130/G52665.1, 2024.

Keir, D., Hamling, I. J., Ayele, A., Calais, E., Ebinger, C., Wright, T. J., Jacques, E., Mohamed, K., Hammond, J. O. S., Belachew, M., Baker, E., Rowland, J. V, Lewi, E., and Bennati, L.: Evidence for focused magmatic accretion at segment centers from lateral dike injections captured beneath the Red Sea rift in Afar, Geology, 37, 59–62, https://doi.org/10.1130/G25147A.1, 2009.

Keir, D., Pagli, C., Bastow, I. D., and Ayele, A.: The magma – assisted removal of Arabia in Afar: Evidence from dike injection in the Ethiopian rift captured using InSAR and seismicity, Tectonics, 30, 1–13, https://doi.org/10.1029/2010TC002785, 2011.

Kidane, T., Courtillot, V., Manighetti, I., Audin, L., Lahitte, P., Quidelleur, X., Gillot, P., Gallet, Y., and Carlut, J.: New paleomagnetic and geochronologic results from Ethiopian Afar: Block rotations linked to rift overlap and propagation and determination of a ∼ 2 Ma reference pole for stable Africa, J. Geophys. Res., 108, https://doi.org/10.1029/2001JB000645, 2003.

La Rosa, A., Pagli, C., Keir, D., Sani, F., Corti, G., Wang, H., and Possee, D.: Observing oblique slip during rift linkage in northern Afar, Geophysical Research Letters, 46, 10782–10790, https://doi.org/10.1029/2019GL084801, 2019.

La Rosa, A., Keir, D., Pagli, C., and Wang, H.: Simultaneous rift-scale inflation of a deep crustal sill network in Afar, East Africa, Nat. Commun., 15, 1–8, https://doi.org/10.1038/s41467-024-47136-4, 2024.

La Rosa, A., Gayrin, P., Brune, S.: Automatic fault maps of the Afar rift and Python workflows for strain calculation, Open Science Framework repository [data set], https://doi.org/10.17605/OSF.IO/AV5WD, 2025.

Lahitte, P., Gillot, P.-Y., Kidane, T., Courtillot, V., and Bekele, A.: New age constraints on the timing of volcanism in central Afar, in the presence of propagating rifts, J. Geophys. Res., 108, https://doi.org/10.1029/2001jb001689, 2003.

Leroy, S., Gente, P., Fournier, M., Acremont, E., Patriat, P., Beslier, M., Bellahsen, N., Maia, M., Blais, A., Perrot, J., Al-kathiri, A., Merkouriev, S., Fleury, J., Ruellan, P., Lepvrier, C., and Huchon, P.: From rifting to spreading in the eastern Gulf of Aden: a geophysical survey of a young oceanic basin from margin to margin, Terra Nov., 16, 185–192, https://doi.org/10.1111/j.1365-3121.2004.00550.x, 2004.

Maestrelli, D., Brune, S., Corti, G., Keir, D., Muluneh, A. A., and Sani, F.: Analog and Numerical Modeling

of Rift-Rift-Rift Triple Junctions, Tectonics, 41, 1–27, https://doi.org/10.1029/2022TC007491, 2022.

Maestrelli, D., Sani, F., Keir, D., Pagli, C., La Rosa, A., Muluneh, A. A., Brune, S., and Corti, G.: Reconciling plate motion and faulting at a rift-rift-rift triple junction, Geology, 1–5, https://doi.org/10.1130/G51909.1, 2024.

Manighetti, I., Tapponnier, P., Gillot, P. Y., Jacques, E., Courtillot, V., Armijo, R., Ruegg, J. C., and King, G.: Propagation of rifting along the Arabia-Somalia plate boundary: Into Afar, J. Geophys. Res., 103, 4947–4974, https://doi.org/10.1029/97JB02758, 1998.

Manighetti, I., Tapponnier, P., Courtillot, V., Gallet, Y., Jacques, E., and Gillot, P.-Y.: Strain transfer between disconnected, propagating rifts in Afar, J. Geophys. Res., 106, 13613–13665, https://doi.org/10.1029/2000JB900454, 2001.

Mattéo, L., Manighetti, I., Tarabalka, Y., Gaucel, J., van den Ende, M., Mercier, A., Tasar, O., Girard, N., Leclerc, F., McClusky, S., Reilinger, R., Ogubazghi, G., Amleson, A., Healeb, B., Vernant, P., Sholan, J., Fisseha, S., Asfaw, L., Bendick, R., and Kogan, L.: Kinematics of the southern Red Sea – Afar Triple Junction and implications for plate dynamics, Geophys. Res. Lett., 37, 1–5, https://doi.org/10.1029/2009GL041127, 2021.

McClusky, S., Reilinger, R., Ogubazghi, G., Amleson, A., Healeb, B., Vernant, P., Sholan, J., Fisseha, S., Asfaw, L., Bendick, R., Kogan L.: Kinematics of the southern Red Sea–Afar Triple Junction and implications for plate dynamics, Geophys. Res. Lett., 37, L05301, https://doi.org/10.1029/2009GL041127, 2010.

Medynski, S., Pik, R., Burnard, P., France, L., Whaler, K., Johnson, N., Benedetti, L., Ayelew, D., Medynski, S., Pik, R., Burnard, P., and France, L.: Stability of rift axis magma reservoirs: Spatial and temporal evolution of magma supply in the Dabbahu rift segment (Afar, Ethiopia) over the past 30 kyr, Earth Planet. Sc. Lett., 409, 278–289, https://doi.org/10.1016/j.epsl.2014.11.002, 2015.

Metzger, S. and Jónsson, S.: Tectonophysics Plate boundary deformation in North Iceland during 1992–2009 revealed by InSAR time-series analysis and GPS, Tectonophysics, 634, 127–138, https://doi.org/10.1016/j.tecto.2014.07.027, 2014.

Moore, C., Wright, T. J., and Hooper, A.: Rift Focusing and Magmatism During Late-Stage Rifting in Afar, J. Geophys. Res.-Sol. Ea., 126, 1–18, https://doi.org/10.1029/2020JB021542, 2021.

Muluneh, A., Brune, S., Pagli, C., La Rosa, A., Keir, D., Neuharth, D., and Corti, G.: To Rotate or to Link? The Connection Between the Red Sea and Gulf of Aden Rifts in Central Afar, Geophys. Res. Lett., 51, e2024GL108732, https://doi.org/10.1029/2024GL108732, 2024.

Neal, J. and Hawker, L.: FABDEM V1-2, University of Bristol [data set], https://doi.org/10.5523/bris.s5hqmjcdj8yo2ibzi9b4ew3sn, 2023.

Neuharth, D., Brune, S., Wrona, T., Glerum, A., Braun, J., and Yuan, X.: Evolution of Rift Systems and Their Fault Networks in Response to Surface Processes, Tectonics, 41, e2021TC007166, https://doi.org/10.1029/2021TC007166, 2022.

Nobile, A., Pagli, C., Keir, D., Wright, T. J., Ayele, A., Ruch, J., and Acocella, V.: Dike-fault interaction during the 2004 Dallol intrusion at the northern edge of the Erta Ale Ridge (Afar, Ethiopia), Geophys. Res. Lett., 39, 2–7, https://doi.org/10.1029/2012GL053152, 2012.

Pagli, C., Wright, T. J., Ebinger, C. J., Yun, S., Cann, J. R., and Barnie, T.: Shallow axial magma chamber at

the slow-spreading Erta Ale Ridge, Nat. Geosci., 5, 1–5, https://doi.org/10.1038/ngeo1414, 2012.

Pagli, C., Wang, H., Wright, T. J., Calais, E., and Lewi, E.: Current plate boundary deformation of the Afar rift from a 3-D velocity field inversion of InSAR and GPS, J. Geophys. Res.-Sol. Ea., 119, 8562–8575, https://doi.org/10.1002/2014JB011391, 2014.

Polun, S. G., Gomez, F., and Tesfaye, S.: Scaling properties of normal faults in the central Afar, Ethiopia and Djibouti: Implications for strain partitioning during the final stages of continental breakup, J. Struct. Geol., 115, 178–189, https://doi.org/10.1016/j.jsg.2018.07.018, 2018.

Rees, R., Gernon, T. M., Keir, D., Taylor, R. N., and Pagli, C.: The spatial and volcanic evolution of Ayelu, Abida and Yangudi volcanoes in the Northern Main Ethiopian Rift – Southern Afar, Ethiopia, J. Volcanol. Geoth. Res., 440, 107846, https://doi.org/10.1016/j.jvolgeores.2023.107846, 2023.

Regenauer-lieb, K., Rosenbaum, G., and Weinberg, R. F.: Strain localisation and weakening of the lithosphere during extension, Tectonophysics, 458, 96–104, https://doi.org/10.1016/j.tecto.2008.02.014, 2008.

Reilinger, R., McClusky, S.: Nubia–Arabia–Eurasia plate motions and the dynamics of Mediterranean and Middle East tectonics, Geophys. J. Int., 186, 971–979, https://doi.org/10.1111/j.1365-246X.2011.05133.x, 2011.

Riedl, S., Melnick, D., Njue, L., Sudo, M., and Strecker, M. R.: Mid-Pleistocene to Recent Crustal Extension in the Inner Graben of the Northern Kenya Rift, Geochem. Geophy. Geosyst., 23, e2021GC010123, https://doi.org/10.1029/2021GC010123, 2022.

Rime, V., Foubert, A., Ruch, J., and Kidane, T.: Tectonostratigraphic evolution and significance of the Afar Depression, Earth-Sci. Rev., 244, 104519, https://doi.org/10.1016/j.earscirev.2023.104519, 2023.

Rime, V., Keir, D., Phethean, J., Kidane, T., and Foubert, A.: Central Afar: An analogue for oceanic plateau development, Geology, 52, 819–824, https://doi.org/10.1130/G52330.1, 2024.

Ruch, J., Keir, D., Passarelli, L., Di Giacomo, D., Ogubazghi, G., and Jonsson, S.: Revealing 60 years of Earthquake Swarms in the Southern Red Sea, Afar and the Gulf of Aden, Front. Earth Sci., 9, 1–20, https://doi.org/10.3389/feart.2021.664673, 2021.

Ruegg, J. C., Lèpin, J. C., and Tarantola, A.: Geodetic measurements of rifting associated with a seismo-volcanic crisis in Afar, Geophys. Res. Lett., 6, 817–820, https://doi.org/10.1029/GL006i011p00817, 1979.

Ruegg, J. C., Kasser, M., and Lépine, J. C.: Strain accumulation across the Asal-Ghoubbet Rift, Djibouti, East Africa, J. Geophys. Res., 89, 6237–6246, https://doi.org/10.1029/jb089ib07p06237, 1984.

Scott, C., Giampietro, T., Brigham, C., Leclerc, F., Manighetti, I., Arrowsmith, J. R., Laó-Dávila, D., and Mattéo, L.: Semiautomatic Algorithm to Map Tectonic Faults and Measure Scarp Height from Topography Applied to the Volcanic Tablelands and the Hurricane Fault, Western US, Lithosphere, 2021, 9031662, https://doi.org/10.2113/2021/9031662, 2021.

Smittarello, D., Grandin, R., Chabalier, J. De, Doubre, C., Deprez, A., Masson, F., Socquet, A., and Saad, I. A.: Transient Deformation in the Asal-Ghoubbet Rift (Djibouti) Since the 1978 Dyking Event: Is Deformation Controlled by Magma

Supply Rates?, J. Geophys. Res.-Sol. Ea., 121, 6030–6052, https://doi.org/10.1002/2016JB013069, 2016.

Stab, M., Bellahsen, N., Pik, R., Quidelleur, X., Ayalew, D., and Leroy, S.: Modes of rifting in magma-rich settings: Tectono-magmatic evolution of Central Afar, Tectonics, 35, 2–38, https://doi.org/10.1002/2015TC003893, 2016.

Stamps, D. S., Kreemer, C., Fernandes, R., Rajaonarison, T. A., and Rambolamanana, G.: Redefining East African Rift System kinematics, Geology, 49, 150–155, https://doi.org/10.1130/G47985.1, 2020.

Stewart, N., Gaudemer, Y., Manighetti, I., Serreau, L., Vincendeau, A., Dominguez, S., Mattéo, L., and Malavieille, J.: "3D_Fault_Offsets," a Matlab Code to Automatically Measure Lateral and Vertical Fault Offsets in Topographic Data: Application to San Andreas, Owens Valley, and Hope Faults, J. Geophys. Res.-Sol. Ea., 123, 815–835, https://doi.org/10.1002/2017JB014863, 2018.

Tarantola, A., Ruegg, J. C., and Lépine, J. C.: Geodetic evidence for rifting in Afar a brittle-elastic model of the behaviour of the lithosphere, Earth Planet. Sc. Lett., 45, 435–444, https://doi.org/10.1016/0012-821X(79)90142-0, 1979.

Tortelli, G., Gioncada, A., Pagli, C., Braschi, E., Gebru, E. F., and Keir, D.: Constraints on the Magma Source and Rift Evolution From Geochemistry of the Stratoid Flood Basalts (Afar, Ethiopia), Geochem. Geophy. Geosyst., 23, 1–21, https://doi.org/10.1029/2022GC010434, 2022.

Tortelli, G., Gioncada, A., Pagli, C., Braschi, E., Gebru, E. F., and Keir, D.: From melt- to crystal-rich magmatic systems during rift localization: Insights from mineral chemistry in Central Afar (Ethiopia), Mineral. Petrol., 7, 179–187, https://doi.org/10.1007/s00410-024-02164-7, 2024.

Tortelli, G., Gioncada, A., Pagli, C., Barford, D. N., Corti, G., Sani, F., Mark, D. F., Dymock, R. C., Gebru, E. F., and Keir, D.: Volcanism records plate thinning driven rift localization in Afar (Ethiopia) since 2–2.5 million years ago, Commun. Earth Environ., 6, 395, https://doi.org/10.1038/s43247-025-02356-4, 2025.

Trippanera, D., J. Ruch, Acocella V., Rivalta E.: Experiments of dike-induced deformation: Insights on the long-term evolution of divergent plate boundaries, J. Geophys. Res.-Sol. Ea., 120, 6913–6942, https://doi.org/10.1002/2014JB011850, 2015.

Varet, J.: Geology of Afar (East Africa), Springer Cham, https://doi.org/10.1007/978-3-319-60865-5, 2018.

Viltres, R., Jonsson, S., Ruch, J., Doubre, C., Reilinger, R., Floyd, M., and Ogubazghi, G.: Kinematics and deformation of the southern Red Sea region from GPS observations, Geophys. J. Int., 221, 2143–2154, https://doi.org/10.1093/gji/ggaa109, 2020.

Viltres, R., Jónsson, S., Alothman, A. O., and Liu, S.: Present-Day Motion of the Arabian Plate, Tectonics, 41, 1–18, https://doi.org/10.1029/2021TC007013, 2022.

Wolfenden, E., Ebinger, C., Yirgu, G., Deino, A., and Ayalew, D.: Evolution of the northern Main Ethiopian rift: birth of a triple junction, Earth Planet. Sc. Lett., 224, 213–228, https://doi.org/10.1016/j.epsl.2004.04.022, 2004.

Wolfenden, E., Ebinger, C., Yirgu, G., Renne, P. R., and Kelley, S. P.: Evolution of a volcanic rifted margin: Southern Red Sea, Ethiopia, GSA Bull., 117, 846–864, https://doi.org/10.1130/B25516.1, 2005.

Wood, A.: Continental Rift Jumps, Tectonophysics, 94, 529–540, https://doi.org/10.1016/B978-0-444-42198-2.50035-3, 1983.

Wright, T. J., Sigmundsson, F., Pagli, C., Belachew, M., Hamling, I. J., Brandsdóttir, B., Keir, D., Pedersen, R., Ayele, A., Ebinger, C., Einarsson, P., Lewi, E., and Calais, E.: Geophysical constraints on the dynamics of spreading centres from rifting episodes on land, Nat. Geosci., 5, 242–250, https://doi.org/10.1038/ngeo1428, 2012.

Wrona, T., Pan, I., Bell, R. E., Jackson, C. A.-L., Gawthorpe, R. L., Fossen, H., Osagiede, E. E., and Brune, S.: Complex fault system revealed by 3-D seismic reflection data with deep learning and fault network analysis, Solid Earth, 14, 1181–1195, https://doi.org/10.5194/se-14-1181-2023, 2023.

Yirgu, G., Ayele, A., and Ayelew, D.: Recent Seismovolcanic Crisis in Northern Afar, Ethiopia, Eos T. Am. Geophys. Un., 87, 325–329, https://doi.org/10.1029/2006EO330001, 2006.

Zielke, O., Arrowsmith, J. R., Ludwing, L. G., and Akçiz, S. O.: Slip in the 1857 and Earlier Large Earthquakes Along the Carrizo Plain, San Andreas Fault, Science, 327, 1119–1122, https://doi.org/10.1126/science.1182781, 2010.

Zunic, J. and Rosin, P. L.: Measuring Linearity of Open Planar Curve Segments, Image Vis. Comput., 29, 873–879, https://doi.org/10.1016/j.imavis.2011.10.002, 2011.

Zunic, J., Pantovi, J., and Rosin, P. L.: Measuring Linearity of Curves, Pattern Recognit., 49, 65–78, https://doi.org/10.1016/j.patcog.2015.07.011, 2016.